

1 **A multivariate spatial interpolation of airborne γ -ray data**

2 **using the geological constraints**

3

4 E. Guastaldi^a, M. Baldoncini^c, G. P. Bezzon^d, C. Brogгинi^b, G. P. Buso^d, A. Caciolli^b,
5 Carmignani L.^a, I. Callegari^a, T. Colonna^a, K. Dule^h, G. Fiorentini^{c,d,e}, M. Kaçeli Xhixha^g,
6 F. Mantovani^{c,e}, G. Massa^a, R. Menegazzo^b, L. Mou^d, C. Rossi Alvarez^b, V. Strati^c, G.
7 Xhixha^{c,d,f}, A. Zanon^d

8

9 ^aCGT Center for GeoTechnologies, University of Siena, Via Vetri Vecchi, 34 - 52027 San Giovanni
10 Valdarno, Arezzo, Italy.

11 ^bIstituto Nazionale di Fisica Nucleare (INFN), Padova Section, Via Marzolo 8 - 35131 Padova, Italy.

12 ^cDepartment of Physics and Earth Sciences, University of Ferrara, Via Saragat, 1 - 44100 Ferrara, Italy.

13 ^dIstituto Nazionale di Fisica Nucleare (INFN), Legnaro National Laboratory, Via dell'Università, 2 - 35020
14 Legnaro, Padova, Italy.

15 ^eIstituto Nazionale di Fisica Nucleare (INFN), Ferrara, Via Saragat, 1 - 44100 Ferrara, Italy.

16 ^fFaculty of Forestry Science, Agricultural University of Tirana, Kodër Kamëz - 1029 Tirana, Albania.

17 ^gUniversity of Sassari, Botanical, Ecological and Geological Sciences Department, Piazza Università 21-
18 07100 Sassari, Italy.

19 ^hFaculty of Natural Sciences, University of Tirana, Bulevardi "Zogu I", Tirana, Albania.

20

21 **Abstract**

22

23 In this paper we present maps of K, eU, and eTh abundances of Elba Island (Italy)
24 obtained with a multivariate spatial interpolation of airborne γ -ray data using the

25 constraints of the geologic map. The radiometric measurements were performed by a
26 module of four NaI(Tl) crystals of 16 L mounted on an autogyro. We applied the
27 collocated cokriging (CCoK) as a multivariate estimation method for interpolating the
28 primary under-sampled airborne γ -ray data considering the well-sampled geological
29 information as ancillary variables. A random number has been assigned to each of 73
30 geological formations identified in the geological map at scale 1:10,000. The non-
31 dependency of the estimated results from the random numbering process has been tested
32 for three distinct models. The experimental cross-semivariograms constructed for
33 radioelement-geology couples show well-defined co-variability structures for both direct
34 and crossed variograms. The high statistical correlations among K, eU, and eTh
35 measurements are confirmed also by the same maximum distance of spatial
36 autocorrelation. Combining the smoothing effects of probabilistic interpolator and the
37 abrupt discontinuities of the geological map, the results show a distinct correlation
38 between the geological formation and radioactivity content. The contour of Mt. Capanne
39 pluton can be distinguished by high K, eU and eTh abundances, while different degrees
40 of radioactivity content identify the tectonic units. A clear anomaly of high K content in
41 the Mt. Calamita promontory confirms the presence of felsic dykes and hydrothermal
42 veins not reported in our geological map. Although we assign a unique number to each
43 geological formation, the method shows that the internal variability of the radiometric
44 data is not biased by the multivariate interpolation.

45

46 **Keywords:**

47

48 Multivariate analysis; Airborne γ -Ray Spectrometry; Collocated Cokriging Interpolator;
49 Elba Island; Natural radioactivity; Geological constraint

50

51 **1. Introduction**

52

53 Airborne γ -ray spectrometry (AGRS) is a fruitful method for mapping natural
54 radioactivity, both in geoscience studies and for purposes of emergency response. One of
55 the principal advantages of AGRS is that it is highly appropriate for large scale
56 geological and environmental surveys (Minty, 2011; Sanderson et al., 2004; Rybach et
57 al., 2001; Bierwirth & Brodie, 2008). Typically, the AGRS system is composed of four
58 4 L NaI(Tl) detectors mounted on an aircraft. For fixed conditions of flight a challenge is
59 to increase the amount of geological information, developing dedicated algorithms for
60 data analysis and spatial interpolation. The full spectrum analysis (FSA) with the non-
61 negative least squares (NNLS) constraint (Caciolli et al., 2012) and noise-adjusted
62 singular value decomposition (NASVD) analysis (Minty & McFadden, 1998) introduces
63 notable results oriented to improve the quality of the radiometric data. On the other hand,
64 the multivariate interpolation has the great potential to combine γ -ray data with the
65 preexisting information contained in geological maps for capturing the geological local
66 variability.

67

68 Elba Island (Italy) is a suitable site for testing a multivariate interpolation applied to
69 AGRS data because of its high lithological variability, excellent exposure of outcropping
70 rocks and detailed geological map. In multivariate statistical analysis, different pieces of

71 information about the particular characteristics of a variable of interest may be better
72 predicted by combining them with other interrelated ancillary information into a single
73 optimized prediction model. This approach improves the results of the spatial
74 interpolation of environmental variables. However, sometimes primary and ancillary
75 variables are sampled by different supports, measured on different scales, and organized
76 in different sampling schemes, which makes spatial prediction more difficult.

77

78 In this study the collocated cokriging (CCoK) was used in a non-conventional way for
79 dealing with the primary (AGRS data) and secondary (geological data) variables when
80 the variable of interest has been sampled at a few locations and the secondary variable
81 has been extensively sampled. Using this approach, we provide the map of natural
82 radioactivity of Elba Island.

83

84 **2. Instruments and methods**

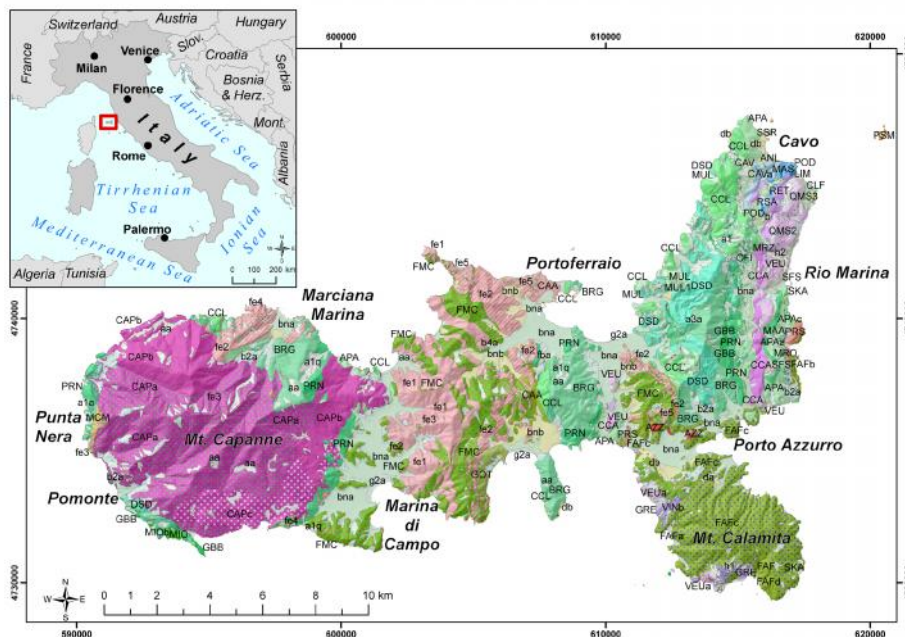
85

86 *2.1. Geological setting*

87

88 Elba is the biggest island of the Tuscan Archipelago and is located in the northern part of
89 the Tyrrhenian Sea, between Italy and Corsica Island (France). It is one of the
90 westernmost outcrop of the Northern Apennines mountain chain (**Figure 1**).

91



92

93 **Figure 1.** Geological map of Elba Island (taken from the Geological Map of Tuscany region realized at
 94 scale 1:10,000, see [CGT, 2011](#)): the western sector is mainly characterized by intrusive igneous rocks
 95 (magenta), the central and eastern sectors are characterized by a wide lithological variation (green, purple,
 96 and pink), while the southeastern outcrop is constituted almost exclusively of metamorphic rocks (Mt.
 97 Calamita). For the legend of the geologic map, see <http://www.geologiatoscana.unisi.it>. The coordinate
 98 system is UTM WGS84 Zone 32 North.

99

100 The geological distinctive features of this island are linked to its complex stack of
 101 tectonic units and the well-known Fe-rich ores, as well as the well-exposed interactions
 102 between Neogene magmatic intrusions and tectonics ([Trevisan, 1950](#); [Bortolotti et al.,](#)
 103 [2001](#); [Dini et al., 2002](#); [Musumeci & Vaselli, 2012](#)). The structure of Elba Island
 104 consists of thrust sheets stacked during the late Oligocene to middle Miocene northern
 105 Apennines deformation. Thrust sheets are cross-cut by late Miocene extensional faults
 106 ([Keller & Coward 1996](#); [Bortolotti et al., 2001](#); [Smith et al., 2011](#)).

107

108 The tectonics of Elba Island is composed of a structural pile of five main units called by
109 **Trevisan (1950)** as “Complexes” and hereafter called “Complexes of Trevisan” (TC): the
110 lowermost three belong to the Tuscan Domain, whereas the uppermost two are related to
111 the Ligurian Domain. **Bortolotti et al. (2001)** performed 1:10,000 mapping of central-
112 eastern Elba and proposed a new stratigraphic and tectonic model in which the five TC
113 were reinterpreted and renamed. TCs are shortly described below.

114

115 The Porto Azzurro Unit (TC I) (Mt. Calamita Unit Auct.) consists of Paleozoic
116 micaschists, phyllites, and quartzites with local amphibolitic horizons, as well as Triassic-
117 Hettangian metasiliciclastics and metacarbonates. Recently **Musumeci et al. (2011)** point
118 out Early Carboniferous age for the Calamita Schist by means of U-Pb and ^{40}Ar - ^{39}Ar
119 radioisotopic data. In particular, in the Porto Azzurro area and the eastern side of Mt.
120 Calamita, the micaschists are typically crosscut by the aplitic and microgranitic dykes
121 that swarm from La Serra-Porto Azzurro monzogranitic pluton (5.1-6.2 Ma, **Dini et al.,**
122 **2010** and references therein). Magnetic activities have produced thermometamorphic
123 imprints in the host rocks (**Garfagnoli et al., 2005; Musumeci & Vaselli, 2012**).

124

125 The Ortano Unit (lower part of TC II) includes metavolcanics, metasandstone, white
126 quartzites and minor phyllites. The Acquadolce Unit (upper part of TC II) is composed of
127 locally dolomitic massive marbles, grading upwards to calcschists (**Pandeli et al., 2001**).
128 This lithology is capped by a thick siliciclastic succession. Ortano and Acquadolce units
129 experienced late Miocene contact metamorphism under low to medium metamorphic
130 grade conditions (**Duranti et al., 1992; Musumeci & Vaselli 2012**).

131

132 The Monticiano-Roccastrada Unit (lower part of TC III) includes basal fossiliferous
133 graphitic metasediments of the Late Carboniferous-Early Permian, unconformably
134 overlain by the detrital Verrucano succession (Middle-Late Triassic) (**Bortolotti et al.,**
135 **2001**). The Tuscan Nappe Unit (central part of TC III) is represented by calcareous-
136 dolomitic breccias and overlying carbonatic outcrops northwards. Most of Grassera Unit
137 (upper part of TC III) is composed of varicolored slates and siltstones with rare
138 metalimestone or meta-chert intercalations; basal calcschists also occur.

139

140 The Ophiolitic Unit (TC IV) is composed of several minor thrust sheets or tectonic sub-
141 units, which are characterized by serpentinites, ophicalcites, Mg-gabbros, and Jurassic-
142 Lower Cretaceous sedimentary cover (**Bortolotti et al., 2001**).

143

144 The Paleogene Flysch Unit (lower part of TC V) mainly consists of shales, marls with
145 limestone, sandstone, and ophiolitic breccia intercalations including fossils of the
146 Paleocene-Eocene age. The Lower-Upper Cretaceous Flysch Unit (upper part of TC V)
147 consists of basal shales and varicolored shales. These lithologies vertically pass to
148 turbiditic siliciclastic sandstones and conglomerates, which in turn alternate with
149 marlstones and marly limestones. Both Flysch Units were intruded by aplitic and
150 porphyritic dykes and laccoliths approximately 7-8 Ma ago (**Dini et al., 2002**).

151

152 The geological structure of the island allows a nearly complete representation of
153 lithologies present in the Northern Apennines mountain chain (**Figure 1**). This feature

154 makes Elba Island a complex system in terms of both geological formations and
155 lithologies. Therefore, it is a formidable research site for applying a multivariate
156 interpolation of radiometric data in relationship to lithological properties.

157

158 *2.2. Experimental setup, survey, and data*

159

160 The AGRS system is a modular instrument composed of four NaI(Tl) detectors (10×10
161 $\times 40$ cm each) with a total volume of 16 L mounted on an autogyro (**Figure 2**). The
162 system is further equipped with a 1 L “upward-looking” NaI(Tl) detector, partially
163 shielded from the ground radiation and used to account for atmospheric radon. Other
164 auxiliary instruments, including the GPS antenna and pressure and temperature sensors,
165 are used to record the position of the AGRS system and to measure the height above the
166 ground using the Laplace formula (**IAEA, 1991**).

167



168



169

170 **Figure 2.** The airborne γ -ray setup (a) mounted on the autogyro (b). The main detector system is inserted in
171 the box under the "upward-looking" detector, which is placed behind the laptop.

172

173 As a survey strategy, we planned to be as perpendicular as possible to the main N-S strike
174 of the geological structures of the area (**Figure 1**). The flight lines were designed in a
175 spiral structure, constrained by the morphology of the terrain (elevations 0÷1010 m
176 a.m.s.l.), starting from the shore and following the heights of the mountains in the
177 counterclock direction (**Figures 6, 7, 8**). The unique region not properly covered by the
178 airborne γ -ray survey is the top of Capanne Mt., because of the cloudy weather
179 conditions. Averaging the flight altitudes recorded every two seconds we have 140 ± 50
180 m (standard deviation). The survey parameters were designed for a cruise speed of
181 approximately 100 km/h, with space lines at most 500 m from one another. For our flight
182 conditions, the detection system is able to measure the signal (97%) coming from a spot
183 area of approximately 600 m radius, even if 90% comes from the half of this radius. In
184 this study, the effect of attenuation of the signal from the biomass (**Schetselaar et al.,**
185 **2000; Carroll & Carroll, 1989**) was neglected since Elba Island is covered by a large
186 extension of rock outcrops and scattered vegetation of Mediterranean scrub.

187

188 The signal is acquired in list mode (event by event) using an integrated electronic module
189 with four independent signal-processing channels and then analyzed offline in 10s
190 intervals. This time interval is chosen such as to optimize the loss in spatial resolution
191 and to reduce the statistical uncertainty to less than 10%. The γ -spectra are calibrated and
192 analyzed using the full spectrum analysis with non-negative least squares (FSA-NNLS)
193 approach as described in **Cacioli et al. (2012)**. According to the FSA method the
194 spectrum acquired during the offline analysis is fitted as a linear combination of the

195 fundamental spectra derived for each radioelement and for background from the
196 calibration process. The abundances are determined applying the non-negative least
197 squares to minimize the χ^2 : the NNLS algorithm reduces the presence of non-physical
198 results, which can lead to systematic errors ([Cacioli et al., 2012](#)).

199

200 Several corrections are applied to the signal measured at different flight altitudes to
201 determine the concentrations of K, eU (equivalent uranium) and eTh (equivalent thorium)
202 at the ground: a) aircraft and cosmic background correction; b) topology correction; c)
203 flying altitude and height correction and d) atmospheric radon correction. The dead time
204 correction was found to be negligible due to relatively low count rates measured during
205 the flight. The background correction is taken into account during the calibration process
206 where the fundamental spectra of the background due to the aircraft and cosmic radiation
207 is estimated. The numeric regional topographic map at 1:10,000 scale of the ground
208 surface has been accounted for the digital elevation model, which has a 10 m spatial
209 resolution. The effects of the steep Elba Island's topography (ranging between 0 m to
210 1010 m a.m.s.l.) are corrected following the method described in [Schwarz et al. \(1992\)](#).
211 Finally, to compute the concentration at the ground surface, the signal is further corrected
212 by an empirical factor obtained by measuring the signal at several altitudes over a flat
213 surface well characterized by ground measurements. The altitude and topography
214 corrections introduce a total systematic uncertainty on the order of 10% in the final
215 results.

216

217 Further corrections are required for eU concentration because the signal coming from
 218 ground uranium is increased by the radon gas in the air. It is evaluated by using the
 219 method of the “upward-looking” detector, following the procedure described in [IAEA](#)
 220 [\(1991\)](#). The atmospheric radon concentration is estimated by analyzing the spectrum
 221 acquired with the “upward-looking” detector, which is calibrated by flying over the
 222 Tyrrhenian sea at the beginning and the end of the survey. The radon concentration has
 223 been calculated for each time interval and was almost stable during the entire flight ($0.2 \pm$
 224 $0.1 \mu\text{g/g}$). Since the ground abundance of eU varies from $0.2 \mu\text{g/g}$ up to $28.0 \mu\text{g/g}$ over all
 225 of Elba Island, the uncertainty concerning the atmospheric radon subtraction for each
 226 single measurement varies from 2% up to 100%: indicatively in average the relative
 227 uncertainty was 23%.

228

229 The relative uncertainties for K, eU, and eTh abundances¹ in the final results are
 230 summarized in [Table 1](#). The systematic relative uncertainties are estimated by combining
 231 the contributions from the altitude and topography corrections and the calibration
 232 process. We emphasize that the data used as input in the CCoK interpolation are taken
 233 into account without experimental uncertainties and that their positions are related to the
 234 center of the spot area.

235

236 [Table 1](#). Experimental relative uncertainties for the measured abundances of K, eU, and eTh.

Radionuclide	Statistical	Systematic
K	7%	14%
eU	8%	~ 30% ^a
eTh	8%	15%

¹ The activity concentrations of $1 \mu\text{g/g}$ U (Th) corresponds to 12.35 (4.06) Bq/kg and 1% K corresponds to 313 Bq/kg.

237 ^a includes the uncertainty related to atmospheric radon correction.
238

239 *2.3. Geostatistical data analysis*

240

241 Geostatistics involves spatial datasets, predicting distributions that characterize the
242 coregionalization between the variables. The CCoK is a special case of cokriging wherein
243 a secondary variable is available at all prediction locations is used to estimate a primary
244 under-sampled variable, restricting the secondary variable search to a local neighborhood.
245 Frequently, the primary and ancillary (secondary) variables are sampled by different
246 supports, measured on different scales, and organized in different sampling schemes,
247 making the spatial prediction more complex. The integration of data that may differ in
248 terms of type, reliability, and scale has been studied in several works. In **Babak &**
249 **Deutsch (2009)**, for instance, this approach is adopted using dense 3D seismic data and
250 test data for an improved characterization of reservoir heterogeneity.

251

252 This approach is also used for mapping soil organic matter (**Pei et al., 2010**), rainfall, or
253 temperature over a territory (**Goovaerts, 1999; Hudson & Wackernagel, 1994**); ground
254 based radiometry data (**Atkinson et al., 1992**); estimating environmental variables, such
255 as pollutants or water tables (**Guastaldi & Del Frate, 2012; Desbarats et al., 2002;**
256 **Hoeksema et al., 1989**); and mapping geogenic radon gas in soil (**Buttafuoco et al.,**
257 **2010**). To date, this method has not been applied to airborne γ -ray measurements
258 integrated with geological data. A multivariate technique for interpolating airborne γ -ray
259 data on the basis of the geological map information is desirable.

260

261 We used the collocated cokriging as a multivariate estimation method for the
262 interpolation of primary under-sampled airborne γ -ray data using a constraint based on
263 the secondary well-sampled geological information. This section briefly describes the
264 theoretical background of CCoK interpolation and its application to airborne γ -ray data
265 using geological constraints.

266

267 *2.3.1. Collocated cokriging: theoretical background*

268

269 Geostatistical interpolation algorithms construct probability distributions that characterize
270 the present uncertainty by the coregionalization among variables (**Wackernagel, 2003**).
271 The CCoK is an interpolation method widely used when applying a linear
272 coregionalization model (LCM) to a primary under-sampled variable $Z_1(x)$ and a
273 secondary widely sampled variable $Z_2(x)$ continuously known at all grid nodes
274 (**Goovaerts, 1997**).

275

276 **Xu et al. (1992)** advanced a definition in which the neighborhood of the auxiliary
277 variable $Z_2(x)$ is arbitrarily reduced to the target estimation location x_0 only. They
278 formulated CCoK as a simple cokriging linked to the covariance structure (**Chiles &**
279 **Delfiner, 1999**):

280

$$281 \quad \rho_{12}(h) = \rho_{12}(0)\rho_{11}(h) \quad (1)$$

282

283 where $\rho_{11}(h)$ is the correlogram of the primary variable $Z_1(h)$ and $\rho_{12}(h)$ is the cross-
 284 correlogram, which quantifies the spatial correlation between the primary (Z_1) and the
 285 secondary (Z_2) data at a distance h .

286 Assuming $Z_1(x)$ to be known, the value of the primary variable Z_1 at target location x_0
 287 is independent of the value of the secondary variable Z_2 if Z_1 and Z_2 have a mean of
 288 zero and a variance of one. In this case, which is called a ‘‘Markov-type’’ model, the cross
 289 covariance functions are proportional to the covariance structure of the primary variable
 290 (Xu et al., 1992; Almeida & Journel, 1994). A strictly CCoK estimator Z_{1CCoK}^{**} at target
 291 location x_0 depends on both the linear regression of the primary variable Z_1 and the
 292 simple kriging variance σ_{SK}^2 , for $\rho = \rho_{12}(0)$ as follows (Chiles & Delfiner, 1999):

293

$$294 \quad Z_{1CCoK}^{**}(x_0) = \frac{(1 - \rho^2)Z_1^*(x_0) + \sigma_{SK}^2 \rho Z_2(x_0)}{(1 - \rho^2) + \rho^2 \sigma_{SK}^2} \quad (2)$$

295

296 where Z_1^* is the kriging estimation of Z_1 at the target location x_0 and the accuracy of the
 297 CCoK estimation is given by

298

$$299 \quad \sigma_{CCoK}^2 = \sigma_{SK}^2 \frac{(1 - \rho^2)}{(1 - \rho^2) + \rho^2 \sigma_{SK}^2} \quad (3)$$

300

301 *2.3.2. Interpolating airborne γ -ray data on geological constraints*

302

303 In our study, we used the CCoK as a multivariate estimation method for the interpolation
304 of airborne γ -ray data using the geological map information. The primary variable $Z_1(x)$
305 refers to the discrete distribution of the natural abundances of K, eU, or eTh (equivalent
306 thorium) measured via airborne γ -ray spectrometry, whereas the secondary variable
307 $Z_2(x)$ refers to the continuous distribution of the geological formations (i.e., the
308 geological map). In this work, these two sets of information are independent of one
309 another. The data gained through airborne γ -ray spectrometry define a radiometric spatial
310 dataset integrating the sample point positions with the natural abundances of K (%), eU
311 ($\mu\text{g/g}$), and eTh ($\mu\text{g/g}$), together with their respective uncertainties.

312

313 The geological map at a 1:10,000 scale ([CGT, 2011](#)), obtained from a geological field
314 survey, covers the entire area in detail. Moreover, the geological map lists 73 different
315 geological formations, defining in this way a categorical variable. For such a large
316 number of variables, the approach based on categorical variables ([Hengl et al., 2007](#);
317 [Pardo-Iguzquiza & Dowd, 2005](#); [Goovaerts, 1997](#); [Rossi et al., 1994](#); [Bierkens &](#)
318 [Burrough, 1993](#); [Journel, 1986](#)) requires a long time for processing and interpretation.
319 Therefore, we had to consider the geological qualitative (categorical) map as a quasi-
320 quantitative constraining variable. In order to study the frequency of sampling we sorted
321 in alphabetical ascending order the geological formations names and assigned to each one
322 a progressive number. We rearranged the frequencies for obtaining normal distributions
323 of the secondary variable (geology). As we show in the following section, this procedure
324 does not affect the final interpolation results. Thus, we spatially conjoined the airborne γ -

325 ray measures to the geological map. This migration of geological data from the
 326 continuous grid (the geological map) to the sample points (the airborne γ -ray measuring
 327 locations) is performed to yield a multivariate point dataset to be interpolated by CCoK.
 328 As shown in **Table 2**, K (%) and eTh ($\mu\text{g/g}$) abundances have a quasi-Gaussian
 329 distributions, whereas eU ($\mu\text{g/g}$) abundance distribution tends to be positively skewed.
 330 The linear correlation is high between pairs of abundance variables (**Figure 3**). Based on
 331 the previous assumptions, the linear correlation coefficient between radioactivity
 332 measures and values arbitrary assigned to geological formations is meaningless.

333

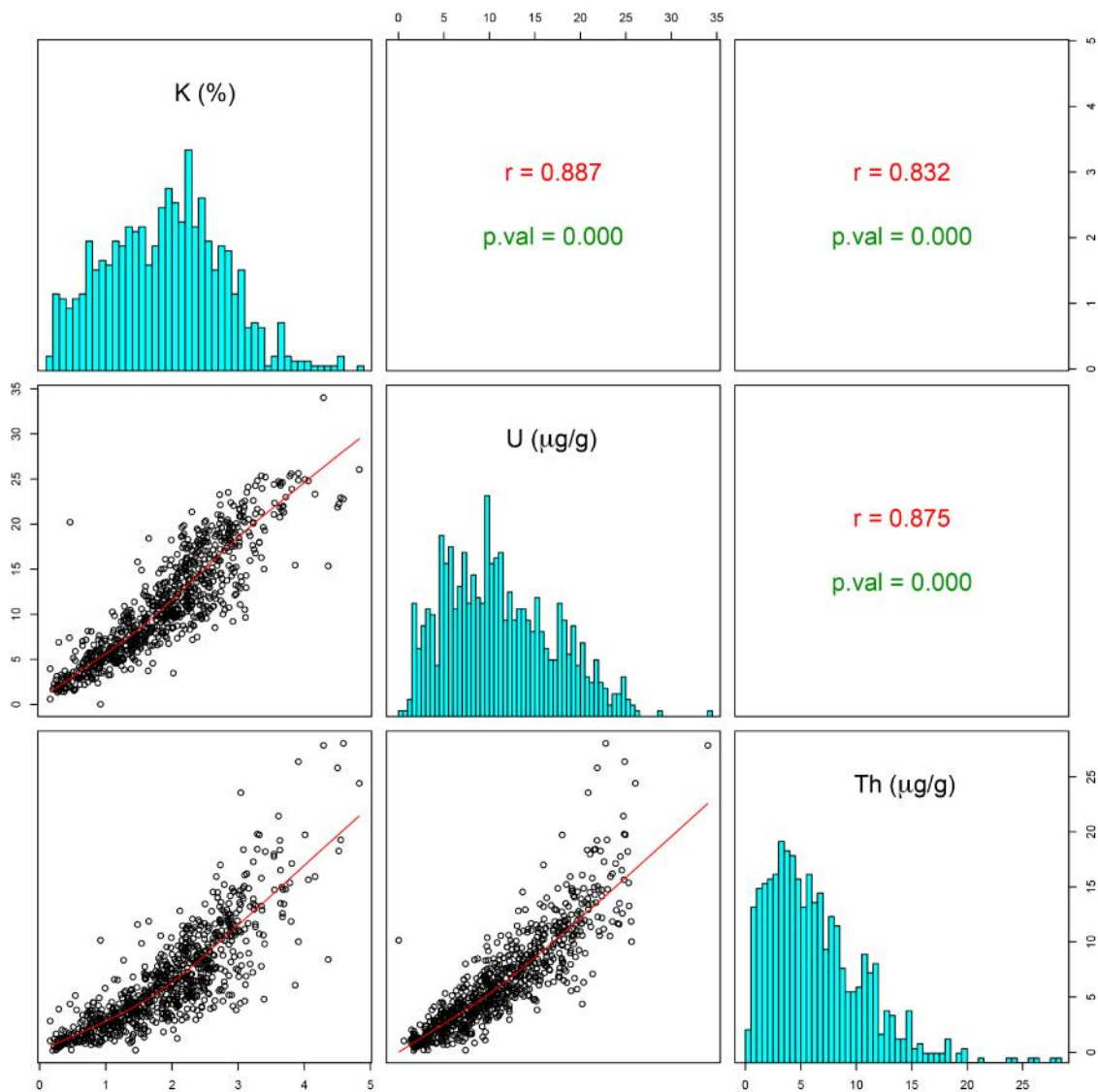
334 **Table 2.** Descriptive statistical parameters of airborne γ -ray data.

Parameter	K (%)	eU ($\mu\text{g/g}$)	eTh ($\mu\text{g/g}$)
Count	806	805	807
Minimum	0.2	0.2	0.03
Maximum	4.8	28.0	34.0
Mean	1.9	6.4	11.1
Std. Dev.	0.9	4.4	5.9
Variance	0.8	19.7	35.2
Variation Coeff.	0.5	0.7	0.5
Skewness	0.2	1.3	0.5

335

336 The CCoK interpolation models, both for the direct spatial correlation and the cross-
 337 correlation of these regionalized variables, were obtained by calculating experimental
 338 semi-variograms (ESV) and experimental cross-semivariograms (X-ESV), and
 339 interpreting the models by taking into account factors conditioning the spatial distribution
 340 of these regionalized variables. The distributions of radioelements of our dataset show a
 341 positive skewness of 0.2, 0.5 and 1.3 for K, eTh and eU respectively (**Table 2**). In the
 342 case of skewness values less than 1, several authors (**Webster & Oliver 2001; Rivoirard**
 343 **2001**) suggest to not perform any normal transformation of the data. Considering that the

344 measurement of eU is contaminated by radon, which increases the experimental
 345 uncertainty, we considered redundant any refinement of data processing. In addition,
 346 supported by well-structured ESVs and X-ESVs for the raw datasets, we didn't perform
 347 any normal transformation for K, eU and eTh.
 348



349
 350 **Figure 3.** Correlation matrix of abundance variables: the lower panel shows the bi-variate scatter plots for
 351 each pair of variables and the robust locally weighted regression (Cleveland, 1979), red line; cells on the
 352 matrix diagonal show the univariate distributions of abundances; the upper panel shows both Pearson's

353 linear correlation coefficient value for each bivariate distribution and the statistical significance testing
354 scores (p-value) for each correlation test.

355

356 The directional X-ESVs show erratic behavior. Therefore, we modeled the experimental
357 co-variability as isotropic, and an omnidirectional LCM has been fitted using a trial-and-
358 error procedure. As shown in **Table 3**, the Gaussian distribution has the mean of
359 standardized errors equal to zero and the variance of standardized errors equal to unity,
360 which allows us to use a cross-validation method. We double-checked the quality of the
361 model (**Clark & Harper, 2000; Goovaerts, 1997; Isaaks & Srivastava, 1989**) by
362 comparing the errors made in estimating airborne γ -ray measures at sample locations with
363 the theoretical standard Gaussian distribution.

364

365 Each group of variables shows the same spatial variability of the geology in the
366 coregionalization matrices because the same parametric variable is still used for all
367 models in the estimation of abundance distribution maps of radioactive elements (**Table**
368 **3**). The result shows a well-structured spherical variability for all groups of variables
369 (**Figure 4**).

370

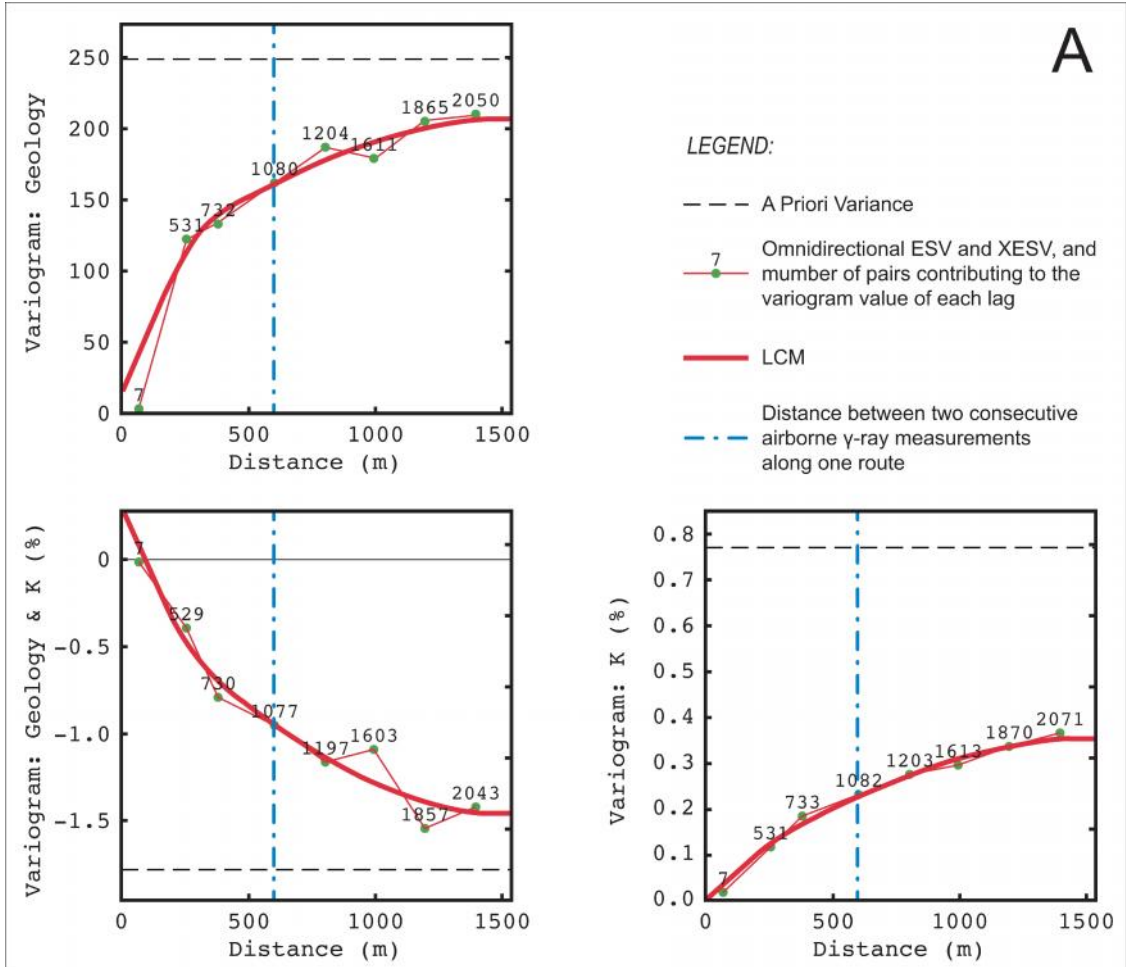
371 **Table 3.** Parameters of linear coregionalization models fitted on omnidirectional variograms calculated
372 with 8 lags of 200 m: groups of primary (radionuclides) and secondary variables; number and types of
373 systems of functions fitted on experimental variograms; range distances for each system of function;
374 matrices of each structure of variability of linear coregionalization model (LCM) fitted for different groups
375 (model values for EVSs in each matrix diagonal cells, model values for XESVs in lower left panel of each
376 matrix; variability values of the parametric geology, in the right column, are unitless); cross-validation

377 results of the fitted LCM (only the primary variables scores are listed; MSE: mean of standardized errors;
 378 VSE: variance of standardized errors) for all groups of variables.

Group of variables	Number and Type of Structures of variability	Range (m)	LCM matrices		Cross-validation		
					MSE	VES	
K & geology	1	Nugget Effect Model	-	0.01 % ²	-	-0.0016	0.68
				0.3 % ²	15		
	2	Spherical Model	400	0.1 % ²	-		
				-0.6 % ²	87		
	3	Spherical Model	1500	0.3 % ²	-		
				-1.2 % ²	105		
eU & geology	1	Nugget Effect Model	-	2.5 µg/g ²	-	-0.00016	0.73
				0.1 µg/g ²	87		
	2	Spherical Model	1500	5.7 µg/g ²	-		
				-5.7 µg/g ²	120		
eTh & geology	1	Nugget Effect Model	-	0.4 µg/g ²	-	-0.0008	0.65
				-0.1 µg/g ²	15		
	2	Spherical Model	400	2.1 µg/g ²	-		
				-0.4 µg/g ²	87		
	3	Spherical Model	1500	11.2 µg/g ²	-		
				-10.6 µg/g ²	105		

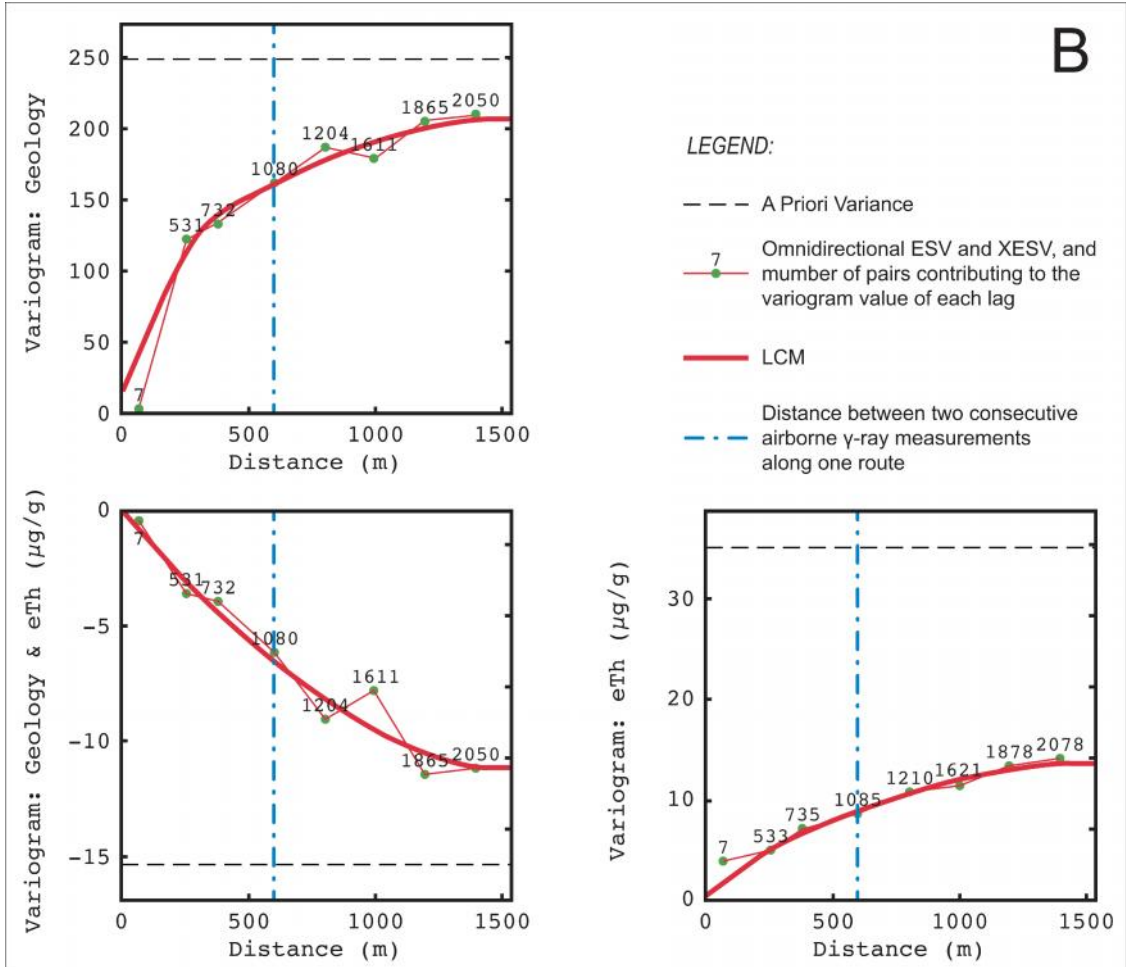
379

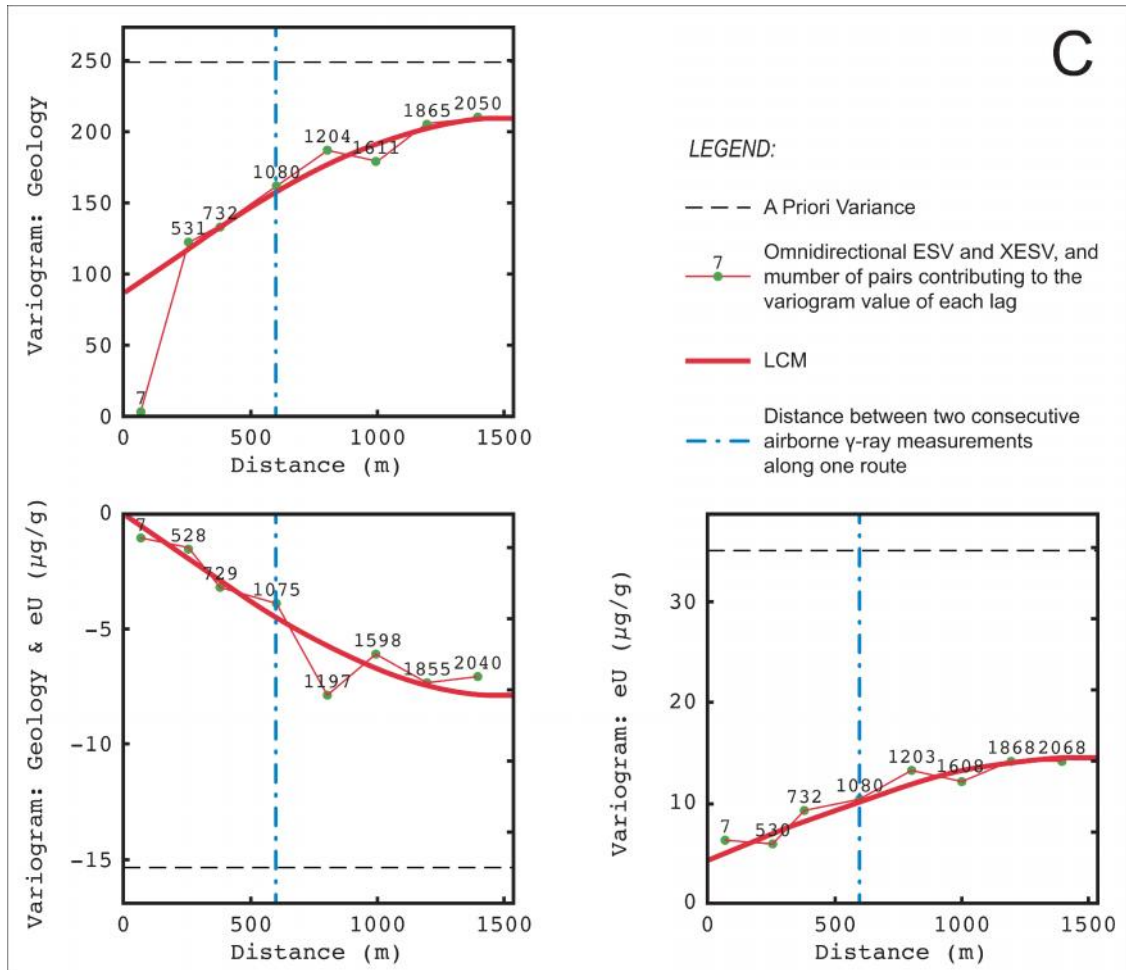
A



380

B





382

383 **Figure 4.** Omnidirectional Linear Coregionalization Model fitted for the experimental semi-variograms
 384 (ESV, on diagonal cells of the matrix) and cross-semivariograms (XESV lower left corner cell) for all
 385 groups of radionuclides and parametric geology: (a) Geology and K; (b) Geology and eTh; (c) Geology and
 386 eU.

387

388 **3. Results and discussion**

389

390 On the 3rd of June, 2010, the autogyro flew over Elba Island (224 km²): during
 391 approximately two hours of flight, the ARGs system collected 807 radiometric data with

392 an average spot area of approximately 0.25 km^2 (source of 90% of the signal). The
393 average altitude of the flight was $140 \pm 50 \text{ m}$.

394

395 Performing the post-processing described in [section 2.2](#), we associated homogenous K,
396 eU, and eTh abundances to each spot area. Considering that 96% of the total 2574
397 geological polygons covering the surface of Elba Island have an area less than 0.25 km^2 ,
398 we observe that many of the airborne γ -ray measurements refer to the contributions
399 coming from several geological formations with different lithological compositions.
400 However, these polygons cover only 25% of the surface of Elba Island. The high density
401 of radioactivity data and the highly refined geological map allowed to construct a well
402 tested LCM: the cross-validation results are shown [Table 3](#). Based on this consistent
403 framework, the multivariate analysis produced data characterized by a good assessment
404 of spatial co-variability. According to the flight plan, the autogyro crossed its own route
405 resulting in a very low variability in the first lags of the omnidirectional co-
406 regionalization model (e.g. ESV of K in [Figure 4 \(a\)](#)). The ESV models referred to
407 AGRS measurements show regular structures with low variability at small distances and
408 generally higher variability at the spherical parts. Indeed, the nugget effect of K
409 abundance contributes almost 2% of the total amount of spatial variability, providing
410 evidence of autocorrelation. The same features are found for the eTh and eU abundances,
411 whose variances at small distances contribute 3% and 30% of the total spatial variation,
412 respectively.

413

414 Moreover, we notice a low spatial variability below 600 m (indicating the spot area
415 radius, indicated by the blue dashed line in **Figure 4**), which corresponds to data obtained
416 by partially overlapping spot areas. The maximum distance of spatial autocorrelation for
417 K, eU, and eTh is 1500 m (**Table 3**), this also due to their high statistical correlation
418 (**Figure 3**). These features reconstructed the spatial resolution of the AGRS survey,
419 confirming the consistency of the model and the AGRS data.

420

421 The variability of the parametric geology variogram at small distances show a weak
422 variability discontinuity at lag $h = 0$, i.e., a nugget effect. This contributes almost 50% of
423 the total spatial variability together with the first range of autocorrelation found at 400 m.
424 This due to either the random values assigned to the categories of the geological map,
425 where a significant difference can be found between the sample values of two adjacent
426 geological formations or in the 600 m spot area radius (**Figure 4**).

427

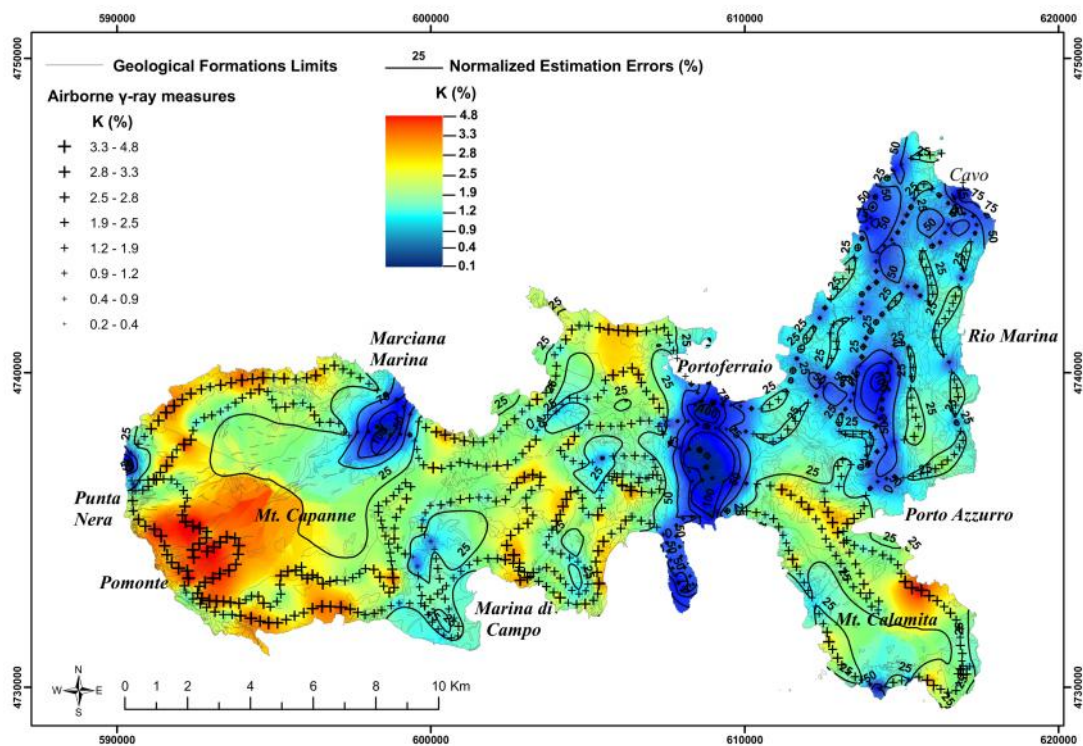
428 The X-ESVs constructed for radioelement-geology couples generally show well-defined
429 co-variability structures. Indeed, both the spherical components of the model are well
430 structured and the contribution of the random part of the variability is always minimized
431 (**Figure 4**). Therefore, we conclude that these choices ensure the consistency of the
432 results achieved by the CCoK multivariate interpolator.

433

434 The estimated maps of the K, eTh, and eU abundances are shown in **Figures 6, 7, and 8**.
435 These maps are calculated with a high spatial resolution (pixel size 10 m x 10 m) in
436 accordance with the choice of the geological map at scale 1:10,000. We also report the

437 accuracy of the estimations in terms of the variance, normalized respect to the estimated
438 values of the abundances (normalized standard deviation, NSD). The percentage
439 uncertainties of the abundances are higher when the absolute measures are smaller, with
440 average NSDs of 27%, 28%, and 29% for K, eU, and eTh, respectively.

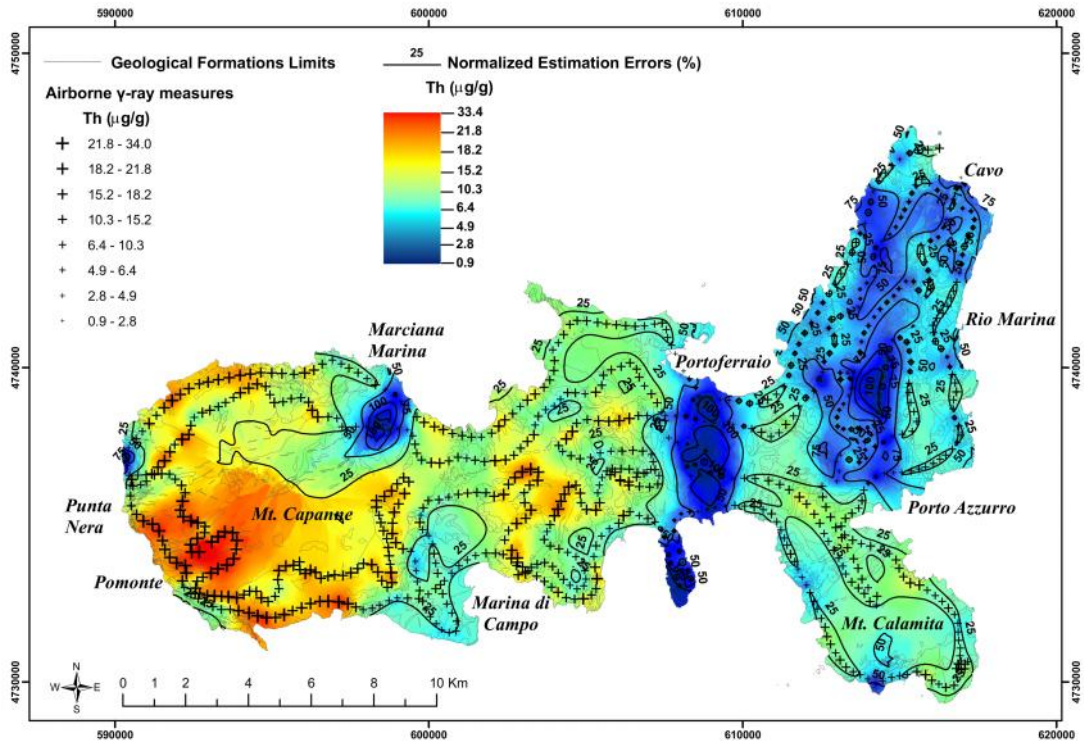
441



442

443 **Figure 5.** Estimation map of K (%) abundance and normalized estimation errors.

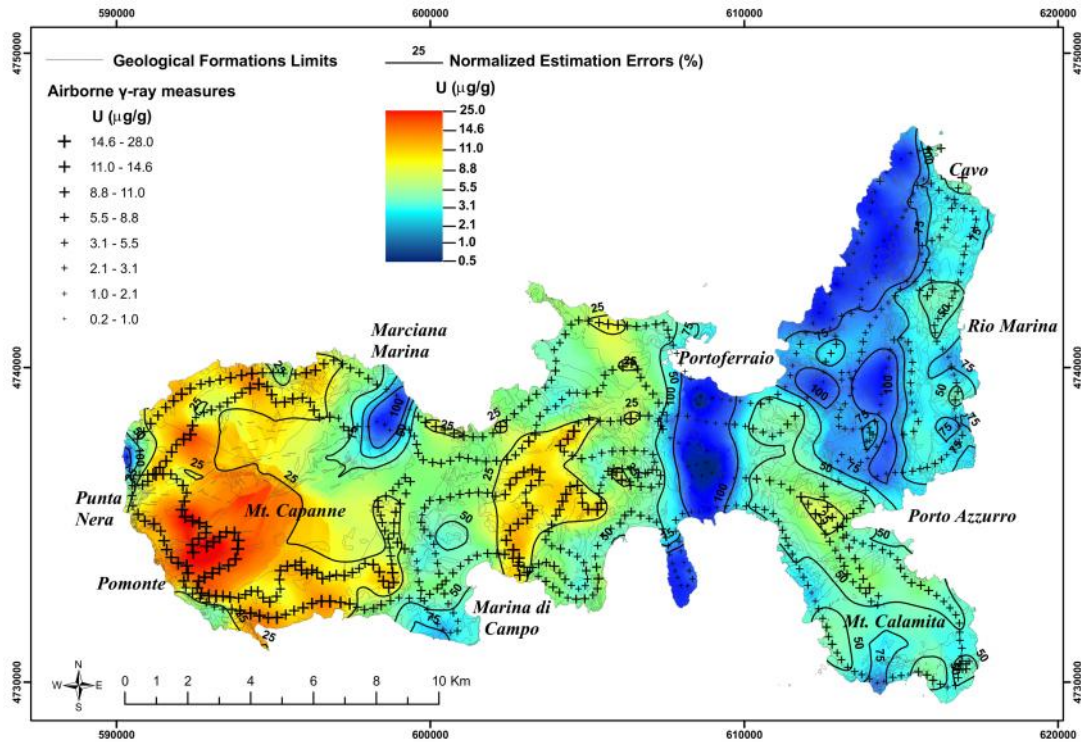
444



445

446 **Figure 6.** Estimation map of eTh ($\mu\text{g/g}$) abundance and normalized estimation errors.

447



448

449 **Figure 7.** Estimation map of eU ($\mu\text{g/g}$) abundance and normalized estimation errors.

450

451 In the geostatistical approach described above, we faced the problem of correlating a
 452 quantitative variable (radioactivity content) to a typical categorical extensive variable
 453 (geological map). As a first solution, the standard Gaussian distribution of the secondary
 454 variable (Geo1) was chosen in a range of values from -10^2 to 10^2 . In order to test possible
 455 bias introduced by the choice of the interval of values, we constructed two different
 456 distributions in the range of values from 1 to 10^2 (Geo2) and from 1 to 10^5 (Geo3). The
 457 main results of these tests are summarized in **Table 4** and **Figure 8**; for the sake of
 458 simplicity, we only compare here the estimated maps of K abundance. However, the
 459 entire procedure for every radioelement combined with the geological parametrical map
 460 has been performed. The normalized differences between pairs of maps realized for

461 different casual geological arrays through CCoK interpolations (**Table 4** and **Figure 9**)
 462 confirm that the random assignment does not introduce any systematic bias. Moreover,
 463 the normalized fluctuations of K abundances estimated by three different models are
 464 contained in a range of less than 5%. The quality of the models is not weakened by the
 465 assignment of random values to geological categories.

466

467 **Table 4.** Descriptive statistics of the CCoK estimation maps of K abundances (unit of measurement: mg/g)
 468 using three different parametric classifications of the geological map (Geo1, Geo2, and Geo3), the
 469 respective estimation errors maps (NSD), and their algebraic map differences (unit of measurement: %).

Type	Geological map	Min.	Max.	Mean	Std. Dev.
CCoK estim.	Geo1	0.15	48.80	19.37	0.79
	Geo2	0.15	48.80	19.37	0.79
	Geo3	0.16	48.24	19.36	0.79
NSD	Geo1	0.79	187.62	27.24	19.58
	Geo2	0.79	217.74	27.24	19.69
	Geo3	6.00	255.00	27.22	19.89
Differ. CCoK	(Geo1-Geo2)/Geo1	-0.33	0.56	-0.001	0.001
	(Geo1-Geo3)/Geo1	-1.84	1.60	-0.004	0.076
	(Geo2-Geo3)/Geo2	-1.72	1.49	-0.007	0.082
Differ. NSD	(Geo1-Geo2)/Geo1	-44.11	91.87	-1.01	-0.88
	(Geo1-Geo3)/Geo1	-85.19	90.55	-0.09	1.21
	(Geo2-Geo3)/Geo2	-34.67	49.03	0.10	0.81

470

471 The main features of the resulting radiometric maps of abundances for the natural
 472 radioelements overlay the prominent geological formations of Elba Island. Indeed, the
 473 relevant geological structures defined by the TCs, described in **section 2.1**, can easily be
 474 identified by comparing similar abundances of natural radioelements.

475

476 The radiometric maps of K, eTh, and eU abundances (**Figures 6, 7, and 8**) show high
 477 values in the western sector of the island, corresponding to the intrusive granitic complex
 478 on Mt. Capanne (indicated as the “CAPa” and “CAPb” geological formations in **Figure**

479 1). In 19 rock samples of Mt. Capanne pluton reported in [Farina et al. \(2010\)](#) the
480 abundances of K, Th, and U are 3.6 ± 0.2 %, 20.8 ± 1.6 $\mu\text{g/g}$ and 8.2 ± 5.1 $\mu\text{g/g}$
481 respectively. The values match with those estimated in [Figure 5, 6 and 7](#). Although the
482 distributions of radioelements do not distinguish among the three intrusive facies, which
483 are mainly characterized by the widespread occurrence of euhedral K-feldspar
484 megacrysts, the area with high content of K, Th and U obtained by multivariate
485 analysis follows the contour map of Mt. Capanne pluton reported in Figure 9a in [Farina](#)
486 [et al. \(2010\)](#). However, the highest content of K, Th and U are localized in the
487 southwestern part of pluton with the maximum concentration in correspondence of the
488 Pomonte valley, SW-NE oriented that is one of the most prominent morphological
489 lineament of western Elba ([Figure 5, 6, and 7](#)). This is an important tectonic lineament
490 crossing all the Mt. Capanne, abruptly separating two different morphological assets: the
491 north-western part shows rough slopes and deep valleys, whilst the south-eastern one is
492 characterized by gently landscape. The hypothesis of an enrichment of radioelements
493 related to this tectonic lineament should be investigated by further airborne and ground
494 surveys.

495

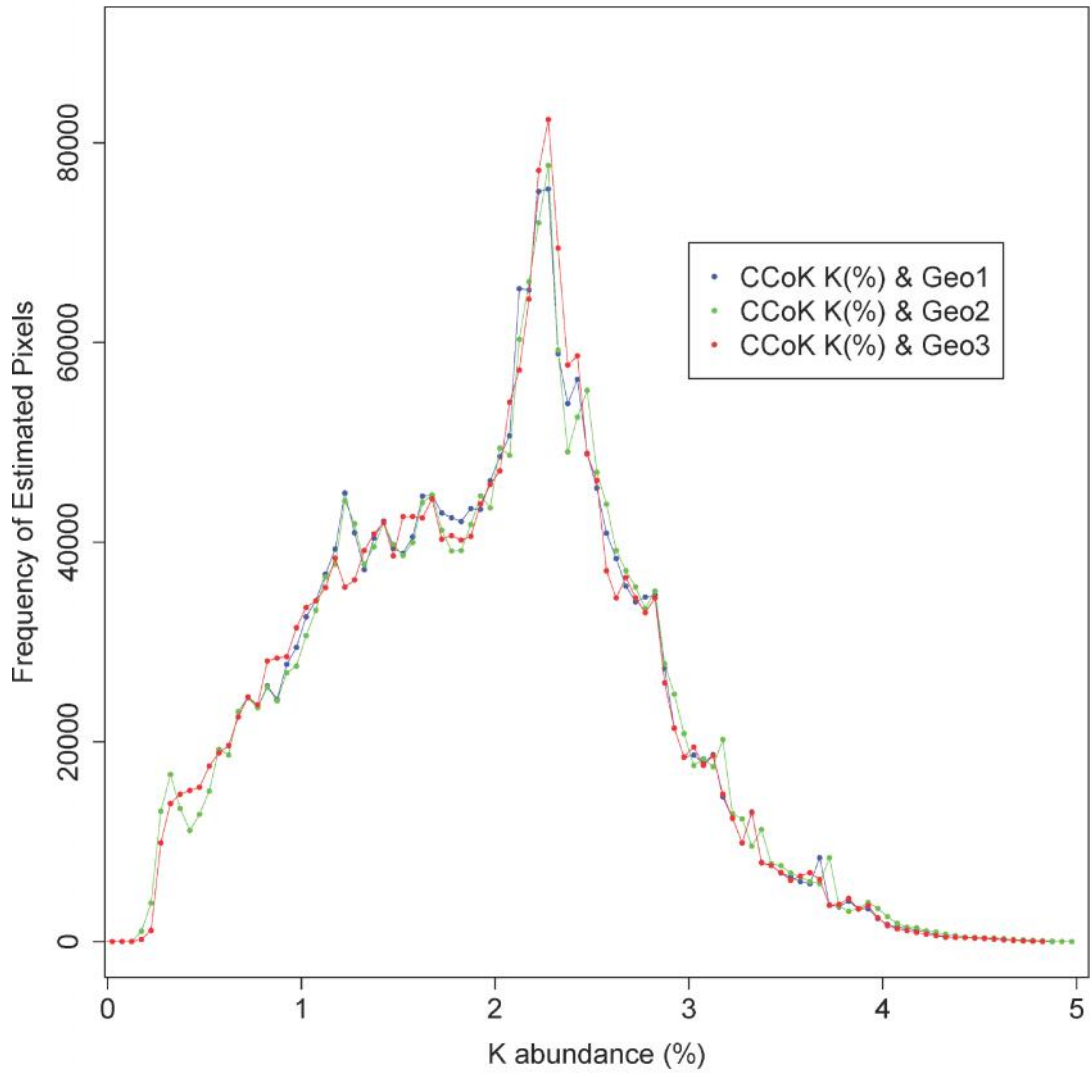
496 As shown in [Figure 5, 6, and 7](#) the geological formations belonging to TC II and TC III
497 have low natural radioelement abundances. The main outcrops are located in the
498 northeastern sector of Elba Island, between Porto Azzurro and Cavo and in the southern
499 part of Portoferraio, where we find peridotites and pillow lavas (indicated as “PRN” and
500 “BRG”, [Figure 1](#)). Finally, low abundance values are found in the area of Punta Nera

501 Cape at the western edge of the Elba Island, where lithologies belonging to the Ophiolitic
502 Unit crop out (TC IV).

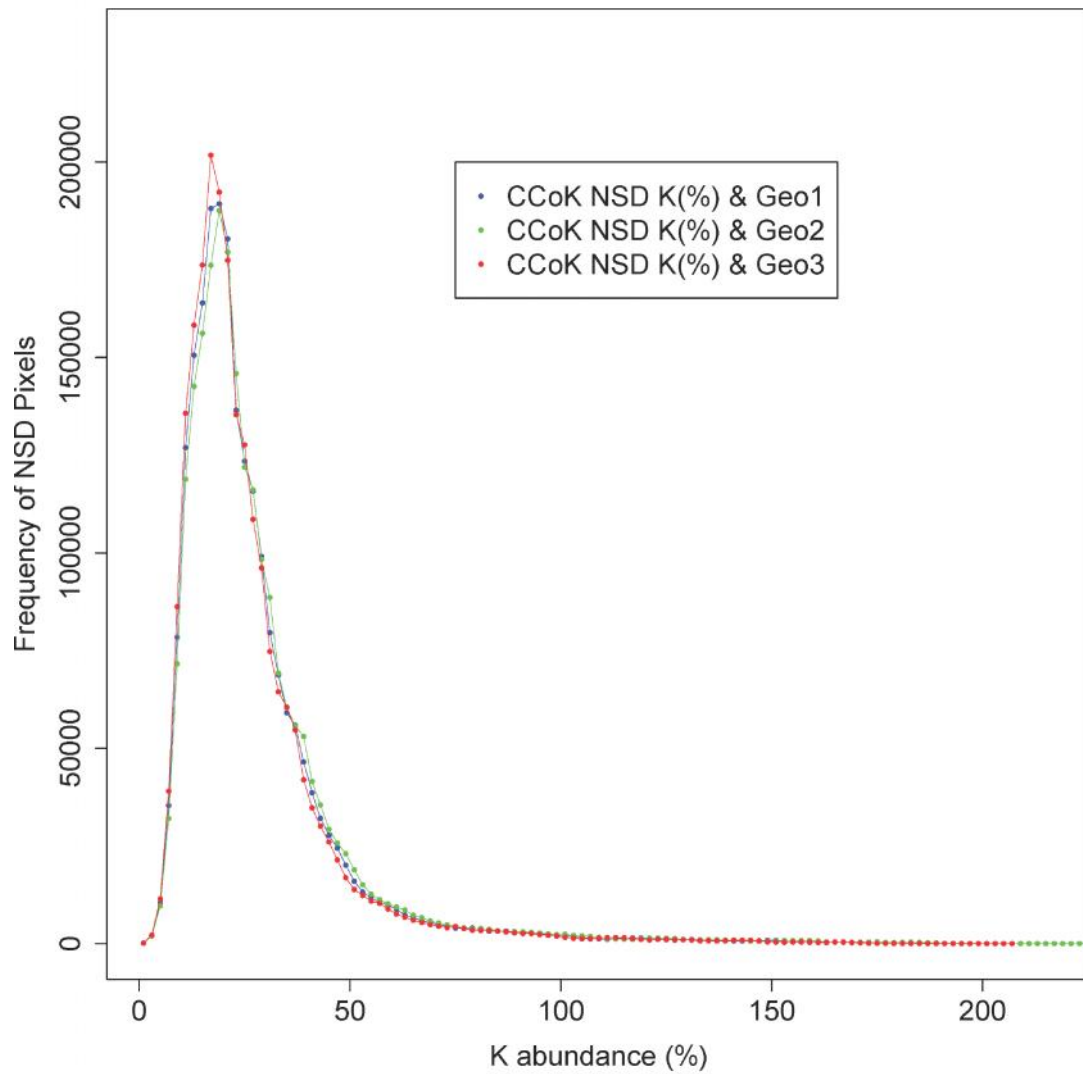
503

504 We emphasize that, although we assign a unique number to each geological formation the
505 internal variability of the radiometric data is not biased by the multivariate interpolation.
506 The main evidence of this feature can be observed inside the polygon including Mt.
507 Calamita, which is identified by a unique geological formation “FAFc” (**Figure 1**). We
508 note a clear anomaly of high K abundance in the northeastern sector of the Mt. Calamita
509 promontory, close to Porto Azzurro (**Figure 5**). This anomaly can be geologically
510 explained considering two related factors. The intense tectonization and following
511 fracturation of this sector allowed a significant circulation of magmatic fluids related to
512 the emplacement of monzogranite pluton of La Serra-Porto Azzurro. Moreover, the
513 presence of felsic dykes, metasomatic masses and hydrothermal veins are recently
514 confirmed by **Dini et al. (2008)** and **Mazzarini et al. (2011)**. Although our geological
515 map doesn't report these lithological details, the quality of radiometric survey is such as
516 to identify the location of the felsic dyke swarm. These dykes 30 - 50 cm thick represent
517 the dominant lithology at the mesoscopic scale and their high frequency in FAFc
518 geological formation contributes to increase the gamma-ray signal. These details are not
519 compromised by the multivariate analysis. The spatial extension of high K content
520 validates the geological sketch reported in **Figure 1** by **Dini et al. (2008)**.

521



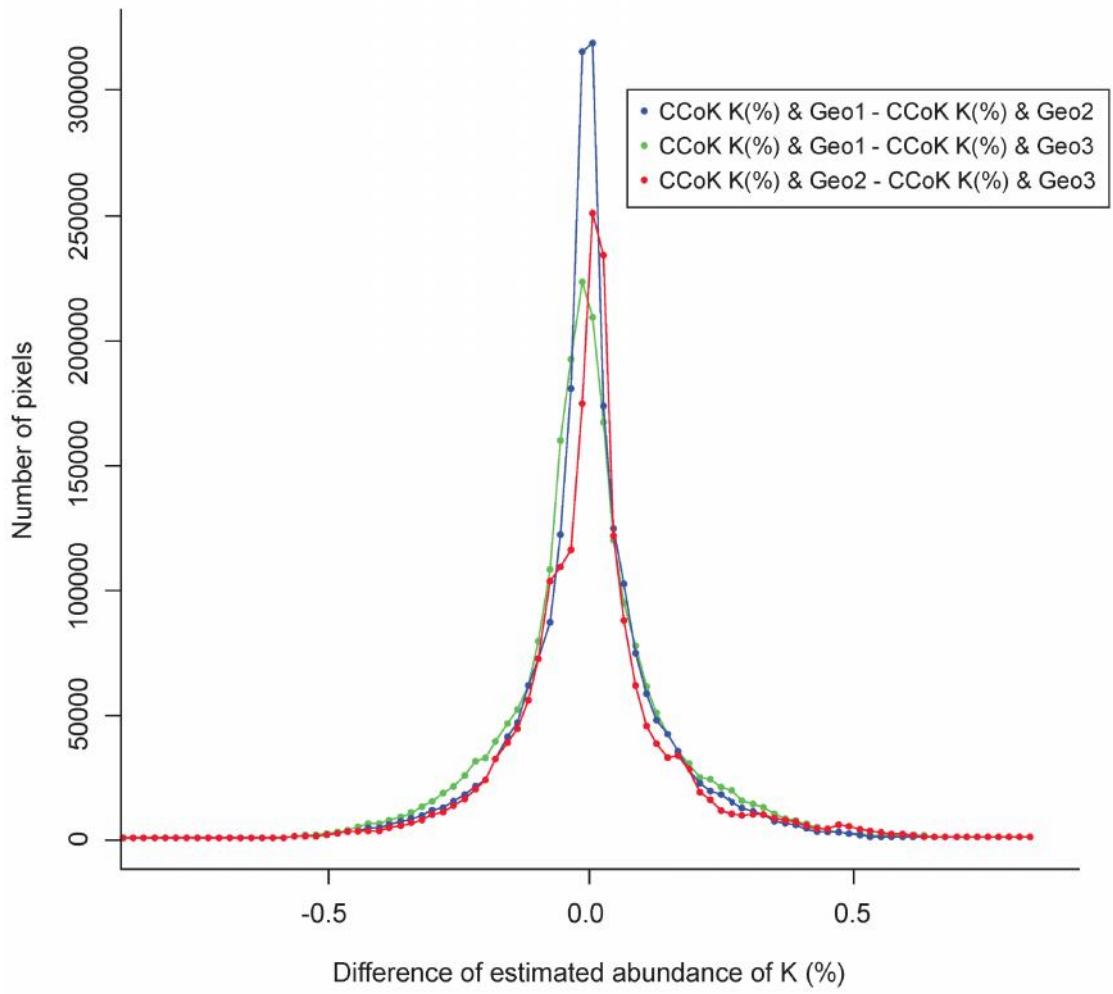
522



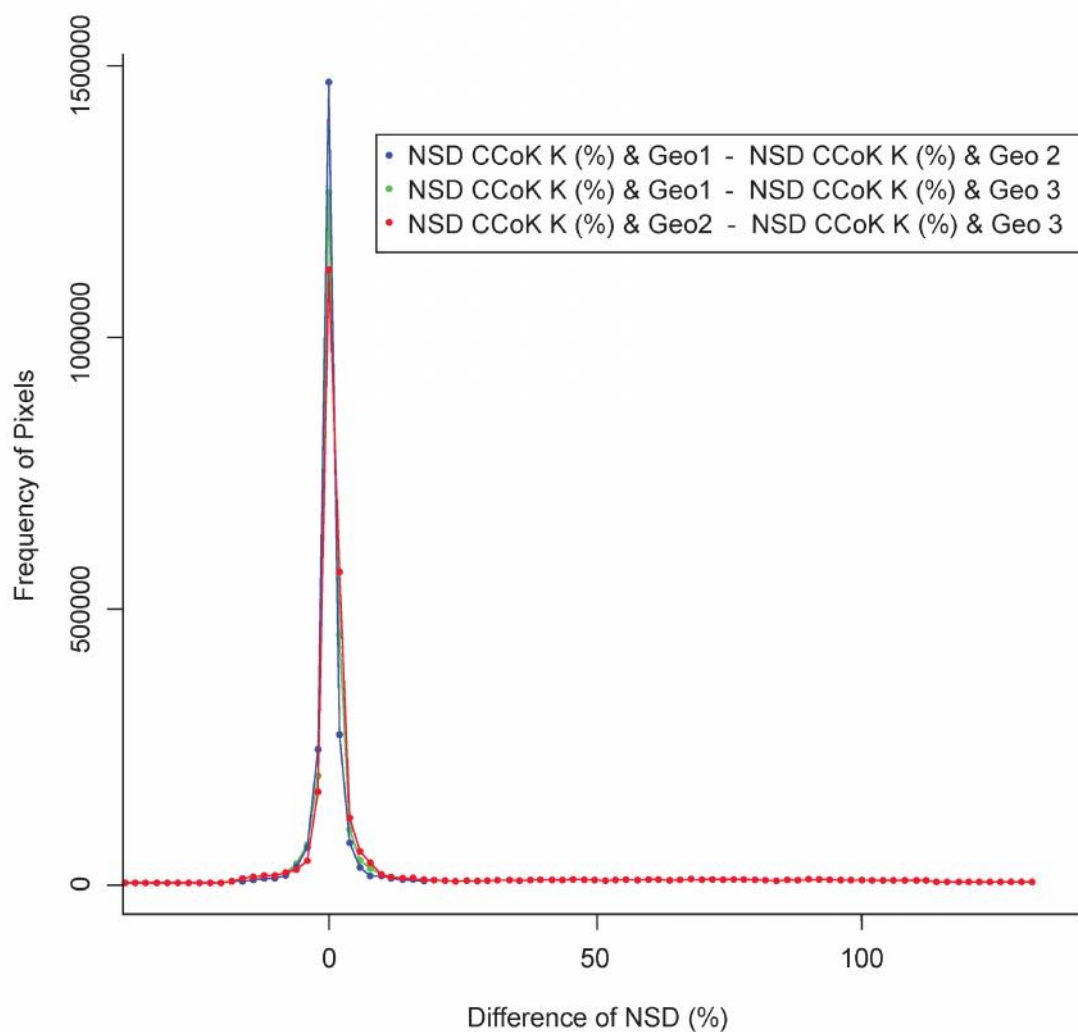
523

524 **Figure 8.** a) Frequency distributions of kriged maps of K abundances estimated by CCoK through three
 525 different reclassifications of the geological map of Elba Island. b) Frequency distributions of the
 526 normalized standard deviation maps (the accuracy of CCoK estimations).

527



528



529

530 **Figure 9.** a) Frequency distributions of the differences between pairs of kriged maps of K abundances
 531 estimated by CCoK through three different reclassifications of geological maps of Elba Island. b)
 532 Frequency distributions of the differences between pairs of normalized standard deviation maps.

533

534 **4. Conclusions**

535

536 In this study we realized the first detailed maps of K, eU, and eTh abundances of Elba
 537 Island showing the potential of the multivariate interpolation based on combination of

538 AGRS data and preexisting information contained in the geological map (at scale
539 1:10,000). We summarize here the main results reached in this study.

540

541 • The multivariate analysis technique of collocated cokriging (CCoK) was applied
542 in a non-conventional way, using the well-sampled geology as a quasi-
543 quantitative variable and constraining parameter. This approach gives a well-
544 structured LCMs which show a good spatial co-variation in the omnidirectional
545 coregionalization ESV model. The ESV models show low spatial variability
546 below 600 m, which also corresponds to the radiometric data obtained by partially
547 overlapped spot areas as well as the autocorrelation distance of 1500 m for the
548 three radionuclides. The ESV model of the geology shows a weak variability
549 discontinuity in the first lag, corresponding to the random assignment of quasi-
550 quantitative values of adjacent geological formations, but also a strong spatial
551 relationship up to the first range of autocorrelation. The procedure of the cross-
552 validation of the model yields a mean close to zero for the standardized errors
553 (MSE) and a variance of standardized errors (VSE) close to unity for all groups of
554 variables.

555 • The CCoK based on the geological constraint was performed by randomly
556 assigning a number to each category of the 73 geological formations. Three
557 different geological quasi-quantitative variable datasets were used, and
558 satisfactory results were achieved by assuring the non-dependency of the model.
559 The normalized fluctuations of three different models are contained in a range of
560 less than 5%.

- 561 • Combining the smoothing effects of the probabilistic interpolator (CCoK), and the
562 abrupt discontinuities of the geological map, we observe a distinct correlation
563 between the geological formation and radioactivity content as well as high K, eU
564 and eTh abundances in the intrusive granitic complex on Mt. Capanne and low
565 abundances in the geological formations belonging to TC II, TC III and TC IV.
- 566 • Although we assign a unique number to each geological formation, the internal
567 variability of the radiometric data is not biased by the multivariate interpolation.
568 The main evidence of this feature can be observed in the northeastern sector of the
569 geological polygon including Mt. Calamita. A clear anomaly of high K content
570 has confirmed the presence of felsic dykes and hydrothermal veins not reported in
571 our geological map, but recently studied ([Dini et al., 2008](#)) as a proxy of the high
572 temperature system currently active in the deep portion of Larderello-Travale
573 geothermal field.

574

575 **Acknowledgements**

576

577 The authors are indebted to E. Bellotti, G. Di Carlo, P. Altair, S. De Bianchi, P. Conti and
578 R. Vannucci for useful suggestions and invaluable discussions. This work has been
579 sponsored by the INFN, Cassa di Credito Cooperativo Padova e Rovigo, and funded by
580 Tuscany Region.

581

582 **References**

583

584 Almeida, A. & Journel, A. (1994). Joint simulation of multiple variables with a markov-type
585 coregionalization model. *Mathematical Geology*, 26(5), 565–588.
586

587 Atkinson P.M., Webster R. & Curran P.J.(1992). Cokriging with ground-based radiometry. *Remote*
588 *Sensing of Environment*, 41 (1), 45–60.
589

590 Babak, O. & Deutsch, C. V. (2009). Improved spatial modeling by merging multiple secondary data for
591 intrinsic collocated cokriging. *Journal of Petroleum Science and Engineering*, 69(1-2), 93–99.
592

593 Bierkens, M. F. P. & Burrough, P. (1993). The indicator approach to categorical soil data: Theory. *Journal*
594 *of Soil Science*, 44, 361–368.
595

596 Bierwirth P.N. & Brodie R.S. (2008). Gamma-ray remote sensing of aeolian salt sources in the Murray–
597 Darling Basin, Australia. *Remote Sensing of Environment*, 112(2), 550–559.
598

599 Bortolotti, V., Fazzuoli, M., Pandeli, E., Principi, G., Babbini, A., & Corti, S. (2001). Geology of central
600 and eastern Elba island, Italy. *Ofioliti*, 26(2a), 97–150.
601

602 Buttafuoco, G., Tallarico, A., Falcone, G., & Guagliardi, I. (2010). A geostatistical approach for mapping
603 and uncertainty assessment of geogenic radon gas in soil in an area of southern Italy. *Environmental Earth*
604 *Sciences*, 61(3), 491–505.
605

606 Caciolli, A., Baldoncini, M., Bezzon, G., Broggin, C., Buso, G., Callegari, I., Colonna, T., Fiorentini, G.,
607 Guastaldi, E., Mantovani, F., Massa, G., Menegazzo, R., Mou, L., Rossi Alvarez, C., Shyti, M., Xhixha, G.,
608 & Zanon, A. (2012). A new FSA approach for in-situ gamma-ray spectroscopy. *Science of The Total*
609 *Environment*, 414, 639–645.
610

611 Carroll S.S. & Carroll T.R. (1989). Effect of forest biomass on airborne snow water equivalent estimates
612 obtained by measuring terrestrial gamma radiation. *Remote Sensing of Environment*, 27(3), 313–319.
613

614 CGT (2011). Accordo di programma quadro ricerca e trasferimento tecnologico per il sistema produttivo -
615 c.1. geologia e radioattività naturale - sottoprogetto a: Geologia (regional framework program for research
616 and technological transfer to industry, c.1. geology and natural radioactivity, sub-project a: Geology).
617 Technical report, CGT Center for GeoTechnologies, University of Siena; Tuscany Region: Italian Ministry
618 of Education, University and Research. For the official legend for the geological formations, see
619 <http://www.geologiatoscana.unisi.it>.
620

621 Chiles, J.-P. & Delfiner, P. (1999). *Geostatistics: modeling spatial uncertainty*. Probability and Statistics
622 Series. John Wiley and Sons, New York; Chichester.
623

624 Clark, I. & Harper, W. V. (2000). *Practical Geostatistics 2000*, Vol. 1. Ecosse North America Llc.,
625 Columbus, Ohio, U.S.A.
626

627 Cleveland, W. S. (1979). Robust locally weighted regression and smoothing scatterplots. *Journal of*
628 *American Statistical Association*, 74, 829–836.
629

630 Desbarats, A. J., Logan, C. E., Hinton, M. J., & Sharpe, D. R. (2002). On the kriging of water table
631 elevations using collateral information from a digital elevation model. *Journal of Hydrology*, 255(1-4), 25–
632 38.
633

634 Dini, A., Innocenti, F., Rocchi, S., Tonarini, S., & Westerman, D. (2002). The magmatic evolution of the
635 late miocene laccolth-pluton-dyke granitic complex of Elba island, Italy. *Geological Magazine*, 139(3),
636 257–279.
637

638 Dini A., Mazzarini F., Musumeci G. & Rocchi S. (2008). Multiple hydro- fracturing by boron-rich fluids in
639 the Late Miocene contact aureole of eastern Elba Island (Tuscany, Italy). *Terra Nova*, 20, 318-326.
640
641 Dini A., Rocchi S., Westerman D. S. & Farina F. (2010). The late Miocene intrusive complex of Elba
642 Island: two centuries of studies from Savi to Innocenti. *Acta Vulcanologica*, 21, 169-190.
643
644 Duranti S., Palmeri R., Pertusati P.C. & Ricci C.A. (1992). Geological evolution and metamorphic
645 petrology of the basal sequences of Eastern Elba (Complex II). *Acta Vulcanologica*, 2, 213-229.
646
647 Farina F., Dini A., Innocenti F., Rocchi S. & Westerman D. S. (2010). Rapid incremental assembly of the
648 Monte Capanne pluton (Elba Island, Tuscany) by downward stacking of magma sheets. *Geological Society
649 of America Bulletin*, 122(9-10), 1463-1479.
650
651 Garfagnoli F., Menna F., Pandeli E. & Principi (2005). The Porto Azzurro Unit (Mt. Calamita promontory,
652 south-eastern Elba Island, Tuscany): stratigraphic, tectonic and metamorphic evolution – *Bollettino della
653 Società Geologica Italiana*, 3, 119-138.
654
655 Goovaerts, P. (1997). *Geostatistics for natural resources evaluation*. Oxford University Press, Oxford, New
656 York. ISBN-13 978-0-19-511538-3.
657
658 Goovaerts, P. (1999). Using elevation to aid the geostatistical mapping of rainfall erosivity. *Catena*, 34,
659 227–242.
660
661 Guastaldi, E. & Del Frate, A. A. (2012). Risk analysis for remediation of contaminated sites: the
662 geostatistical approach. *Environmental Earth Sciences*, 65(3), 897-916.
663
664 Hengl, T., Toomanian, N., Reuter, H. I., & Malakouti, M. J. (2007). Methods to interpolate soil categorical
665 variables from profile observations: lessons from Iran. *Geoderma*, 140(4), 417–427.

666

667 Hoeksema, R., Clapp, R., Thomas, A., Hunley, A., Farrow, N., & Dearstone, K. (1989). Cokriging model
668 for estimation of water table elevation. *Water Resources Research*, 25(3), 429–438.

669

670 Hudson, G. & Wackernagel, H. (1994). Mapping temperature using kriging with external drift: theory and
671 an example from Scotland. *International Journal of Climatology*, 14, 77–91.

672

673 IAEA, (1991). Airborne gamma-ray spectrometry surveying. Technical Report Series 323, International
674 Atomic Energy Agency, Vienna.

675

676 Isaaks, E. H. and Srivastava, R. M. (1989). *Applied Geostatistics*. Oxford University Press, Oxford, New
677 York.

678

679 Journel, A. (1986). Constrained interpolation and qualitative information. *Mathematical Geology*, 18(3),
680 269–286.

681

682 Keller, J. V. A. and Coward, M. P. (1996). The structure and evolution of the Northern Tyrrhenian Sea
683 *Geological Magazine*, 133, 1-16

684

685 Mazzarini, F. Musumeci, G., Cruden, A. R. (2011). Vein development during folding in the upper brittle
686 crust: The case of tourmaline-rich veins of eastern Elba Island, northern Tyrrhenian Sea, Italy. *Journal of*
687 *Structural Geology*, 33(10), 1509-1522.

688

689 Minty, B. R. S. (2011). Airborne geophysical mapping of the Australian continent. *Geophysics*, 76(A27).

690

691 Minty B. & McFadden P. (1998). Improved NASVD smoothing of airborne gamma-ray spectra.
692 *Exploration Geophysics* 29(4), 516-523.

693

694 Musumeci G., Mazzarini F., Tiepolo M. & Di Vincenzo G. (2011). U-Pb and ^{40}Ar - ^{39}Ar geochronology of
695 Palaeozoic units in the northern Apennines: determining protolith age and alpine evolution using the
696 Calamita Schist and Ortano Porphyroid. *Geological Journal* 46, 288-310.
697
698 Musumeci G. & Vaselli L. (2012). Neogene deformation and granite emplacement in the metamorphic
699 units of northern Apennines (Italy): insights from miloniti marbles in the Porto Azzurro pluton contact
700 aureole (Elba Island). *Geosphere*, 8(2), 470-490.
701
702 Pandeli E., Puxeddu M. & Ruggieri G. (2001). The metasiliciclastic-carbonate sequence of the Acquadolce
703 Unit (eastern Elba Island): new petrographic data and paleogeographic interpretation. *Ofioliti*, 26(2a), 207-
704 218.
705
706 Pardo-Iguzquiza, E. & Dowd, P. A. (2005). Multiple indicator cokriging with application to optimal
707 sampling for environmental monitoring. *Computers and Geosciences*, 31(1), 1–13.
708
709 Pei, T., Qin, C.-Z., Zhu, A.-X., Yang, L., Luo, M., Li, B., & Zhou, C. (2010). Mapping soil organic matter
710 using the topographic wetness index: A comparative study based on different flow-direction algorithms and
711 kriging methods. *Ecological Indicators*, 10(3), 610–619.
712
713 Rivoirard, J. (2001). Which models for Collocated Cokriging? *Mathematical Geology*, 33, 117-13.
714
715 Rossi R.E., Dungan J.L. & Beck L.R. (1994). Kriging in the shadows: Geostatistical interpolation for
716 remote sensing. *Remote Sensing of Environment*, 49(1), 32–40.
717
718 Rybach L., Bucher B. & Schwarz G. (2001). Airborne surveys of Swiss nuclear facility sites. *Journal of*
719 *Environmental Radioactivity*, 53, 291-300.
720

721 Sanderson, D., Cresswell, A., Hardeman, F., & Debauche, A. (2004). An airborne gamma-ray spectrometry
722 survey of nuclear sites in Belgium. *Journal of Environmental Radioactivity*, 72, 213–12.
723

724 Schetselaar E.M., Chung C-J.F. & Kim K.E. (2000). Integration of Landsat TM, Gamma-Ray, Magnetic,
725 and Field Data to Discriminate Lithological Units in Vegetated Granite-Gneiss Terrain. *Remote Sensing of*
726 *Environment*, 71(1), 89–105.
727

728 Schwarz, G., Klingele, E., & Rybach, L. (1992). How to handle rugged topography in airborne gamma-ray
729 spectrometry surveys. *First Break*, 10 (1), 11–17.
730

731 Smith S.A.F., Holdsworth R.E. & Colletini C. (2011). Interactions between low-angle normal faults and
732 plutonism in the upper crust: Insights from the Island of Elba, Italy. *Geological Society of America*
733 *Bulletin*, 123, 329-346.
734

735 Trevisan, L. (1950). L'Elba orientale e la sua tettonica di scivolamento per gravità. *Mem. Ist. Geol. Univ.*
736 *Padova*, 16:5–35.
737

738 Wackernagel, H. (2003). *Multivariate Geostatistics: An Introduction With Applications* (3rd ed.). Springer-
739 *Verlag*, Berlin, Germany.
740

741 Webster, R., & Oliver, M. (2001). *Geostatistics for Natural Environmental Scientists*. John Wiley & Sons,
742 Chichester. ISBN 0-471-96553-7.
743

744 Xu, W., Tran, T., Srivastava, R., & Journel, A. (1992). Integrating seismic data in reservoir modeling: The
745 collocated cokriging alternative. In *SPE Annual Technical Conference and Exhibition*, page., Washington,
746 D.C. Society of Petroleum Engineers Inc.